Presentation of the Small Baselin NSBAS Processing Chain on a Case Example : The Etan Deformation Monitoring from 2003 to 2010 Using Envisat Data

Marie-Pierre Doin, Felicity Lodge, Stephane Guillaso, Romain Jolivet, Cécile Lasserre, Gabriel Ducret, Raphael Grandin, Erwan Pathier, Virginie Pinel

HAL Id: hal-02185213
https://ens.hal.science/hal-02185213

Submitted on 10 Feb 2021

PRESENTATION OF THE SMALL BASELINE NSBAS PROCESSING CHAIN ON A CASE EXAMPLE: THE ETNA DEFORMATION MONITORING FROM 2003 TO 2010 USING ENVISAT DATA

Marie-Pierre Doin[1], Felicity Lodge[3], Stéphane Guillaso[2], Romain Jolivet[3], Cécile Lasserre[3], Gabriel Ducret[1], Raphael Grandin[1], Erwan Pathier[3], and Virginie Pinel[4]

[1]*Ecole Normale Superieure, 24 rue Lhomond, 75005 Paris, France.*
[2]*Technische Universitt Berlin,Franklinstrae 28/29,D-10587 Berlin,Germany.*
[3]*ISTerre BP 53,38041 Grenoble Cedex 9, France.*
[4]*ISTerre-Universit de Savoie, 73376 Le Bourget du Lac Cedex, France.*

ABSTRACT

We assemble a processing chain that handles InSAR computation from raw data to time series analysis. A large part of the chain (from raw data to geocoded unwrapped interferograms) is based on ROI_PAC modules (Rosen et al., 2004), with original routines rearranged and combined with new routines to process in series and in a common radar geometry all SAR images and interferograms. A new feature of the software is the range-dependent spectral filtering to improve coherence in interferograms with long spatial baselines. Additional components include a module to estimate and remove digital elevation model errors before unwrapping, a module to mitigate the effects of the atmospheric phase delay and remove residual orbit errors, and a module to construct the phase change time series from small baseline interferograms (Berardino et al. 2002). This paper describes the main elements of the processing chain and presents an example of application of the software using a data set from the ENVISAT mission covering the Etna volcano.

Key words: InSAR; SBAS; Time series analysis; Etna.

1. INTRODUCTION

The detection of slow, time-dependent ground motion using the InSAR technique requires the analysis and combination of multiple radar data takes over an extended time period. Processing individual image pairs, one at a time, becomes difficult and time consuming when exploiting the large amount of data in the archive of recent missions (ERS, Envisat, RADARSAT). This task will become even greater with future missions like Sentinel-1 with a return period of 12 days. The NSBAS package is a fully automatic chain of processing producing a time-lines of the line of sight surface movement over an area. It has been especially optimized for the monitoring of tran-

sient ground motion of small amplitude, taking place over large areas and in natural settings. In the next sections we synthethize the various features of the chain and refer to publications for the original description and discussion of the software components applied to various natural processes. The NSBAS processing chain is depicted in a flow diagram in Fig. 1. In the present paper, it is applied to the study of the Geohazards Supersite of Mount Etna volcano using Envisat data from an ascending track (Fig. 2) This dataset has been well studied and provides us with a good case example. It consists of 63 SAR data between 2003 and 2010.

2. RAW TO DIFFERENTIAL INTERFEROGRAMS

The first step goes from raw data to differential interferograms. All SLCs (Single Look Complex images) are computed in a common Doppler centroid geometry, chosen to maximize the Doppler bandwidth overlap between images, and band-pass filtered in azimuth. All slave SLCs are re-sampled in a single master SLC geometry using an a priory distortion map in range derived from precise orbits and digital elevation model (DEM), combined with empirical offsets between slave and master images obtained by amplitude image matching. This option will be added to ROI_PAC and distributed with the next version of the package (http://www.openchannelsoftware.com/projects/ROI_PAC). A new feature of NSBAS is the range spectral filter adapted to terrain slope (Guillaso et al., 2011), applied to the SLCs before producing differential interferograms. These improvements from the current version of ROI_PAC processing increase the coherence for large perpendicular baselines (350-500m) and in areas of large relief (Fig. 3).

An optimal small baseline network of interferograms is then defined using temporal and perpendicular baseline constraints. The chosen network is the result of a com-
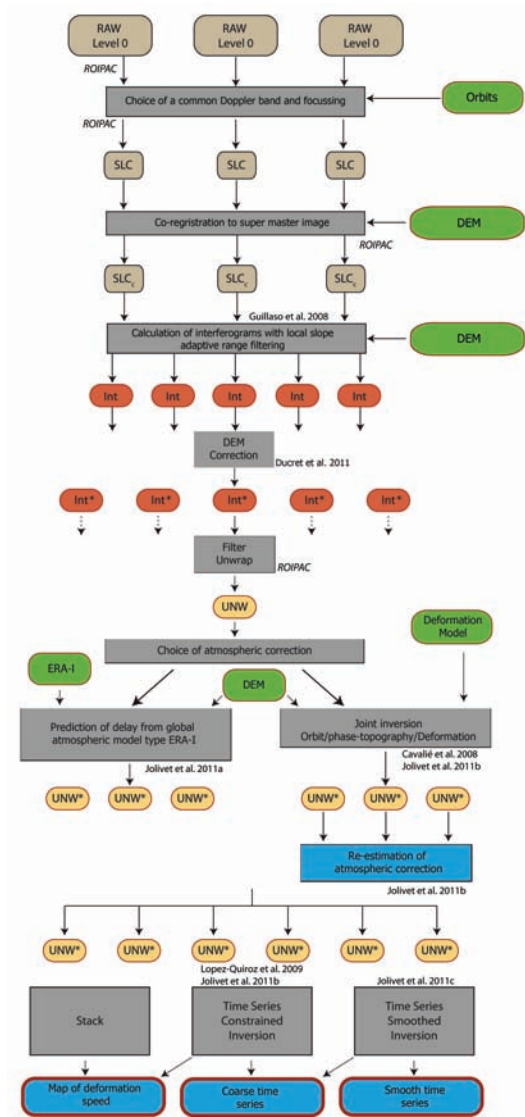
Figure 1. Diagram showing the NSBAS chain steps (Romain Jolivet, thesis)

Figure 2. Topographic map of Sicili. Boxes indicate coverage of Envisat scenes on ascending and descending tracks. Only data from ascending (east looking) track are used in this study. Dots indicate location of ERAI grid nodes.

promise between interferogram redundancy and processing constraints. Interferometric redundancy allows error propagation through the network to be avoided. For the study of Etna, 222 interferograms were computed with perpendicular baselines smaller than 500 m and temporal baselines smaller than 1.3 years (Fig. 4).

3. INTERFEROGRAM FILTERING, UNWRAPPING AND CORRECTIONS

The second step involves phase filtering, unwrapping, and correction of interferograms from atmospheric, orbital and DEM errors. The order in which the various tasks are performed depends on the characteristics of the data set. Unwrapping and filtering the phase before the various correction modules seems to work well in areas
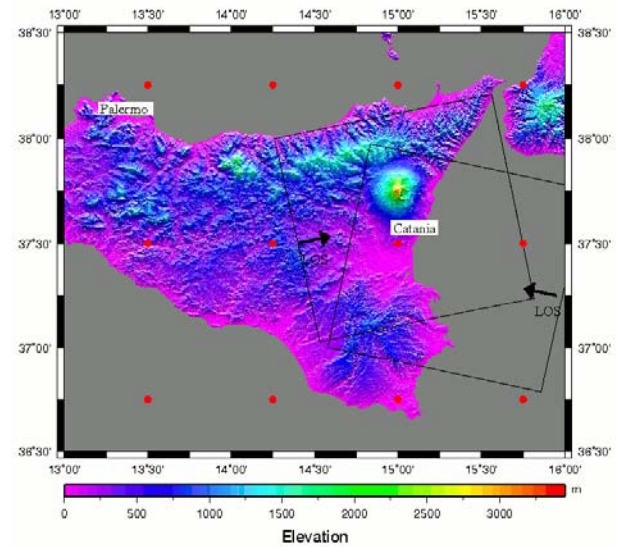
where the coherence is high and the relief moderate (Jolivet et al., 2011b). However, in areas of severe topography (e.g., Mt Etna) it becomes critical to remove the stratified atmospheric signal and the DEM errors from the wrapped phase, then filter and unwrap the corrected phase. This approach proved effective at unwrapping Envisat interferograms across the Himalaya between the Tibetan Plateau and the Ganga Valley (Grandin et al., 2011).

Two options are offered to perform the atmospheric corrections. First the stratified phase delay can be estimated empirically by adjusting a linear or quadratic function to the phase (wrapped or unwrapped) - elevation bivariate set, possibly slowly varying with azimuth for very long scenes. Alternatively, stratified atmospheric effects can be a priori corrected using the ECMWF (European Cen-
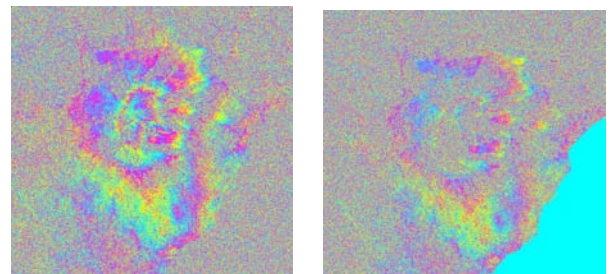

Figure 3. Comparison of wrapped interferograms produced by NSBAS (left) and ROI_PAC (right) for image pair 20100609-20100922 with a perpendicular baseline of 460 m. One colour cycle corresponds to 2.8 cm of phase signal.
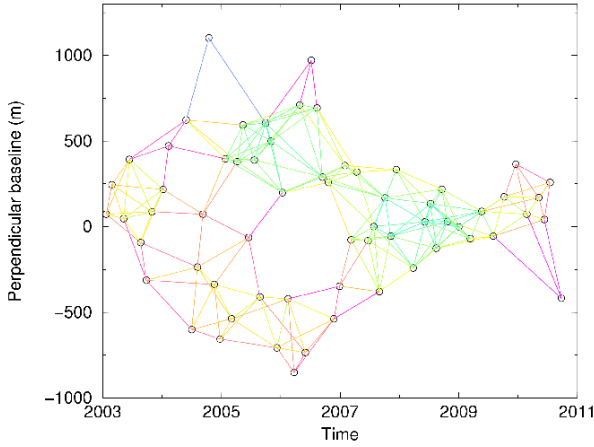
Figure 4. Network of computed small baseline interferograms showing in colour (from blue to green) increasing redundancy, defined through the data covariance matrix. All highly redundant interferograms with large baseline have been removed.
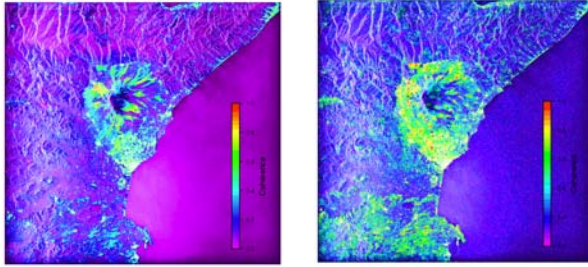

Figure 6. Average spatial coherence (left) and temporal coherence (right) for the set of interferograms processed in this study by the DEM error estimation module.
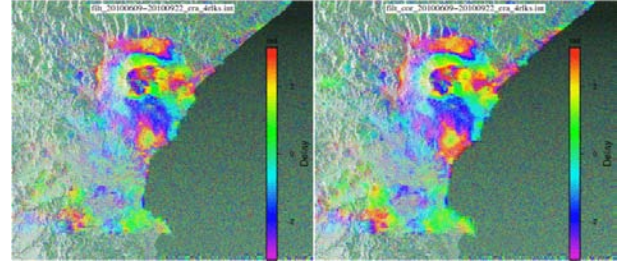

Figure 7. Filtered, wrapped interferogram without (left) or with (right) local DEM error correction. Example of image pair 20100609_20100922 with a perpendicular baseline of 460 m. The effect of DEM error correction on retrieved coherence is mainly visible in the mountains in the far field (e.g., south west or north east part of the image).

tre for Median-Range Weather Forecast) ERAI (ERA-Interim) atmospheric reanalysis (Fig. 5), an approach validated in Doin et al. (2009) and in Jolivet et al. (2011a). The use of an external atmospheric model is preferable when the deformation is expected to correlated with the elevation, as in the case of the Etna volcano (Beauducel et al., 2000).

The local DEM errors and temporal coherence (Fig. 6) are estimated on the series of wrapped interferograms, chosen with a threshold on temporal baselines (less than 80 days in the Etna case) (Ducret et al., 2011). Comparison with the average spatial coherence map shows that punctual urban structures may be selected as temporally coherent pixels. Because of high deformation gradients, the methodology used here for estimating DEM errors is not optimal. Nevertheless, DEM error corrections result in increased coherence in mountainous areas away from the volcano (Fig. 7).

Various filters can be used, including simple looking and the adaptative filter of Goldstein and Werner (1998), or a coherence dependent filter that is a weighted average of the complex phase in sliding windows. One option allows adaptative weighting of the filtered phase obtained with various window sizes using the coherence computed in each window. This averaging filter, although crude, allows the retrieval of useful phase information from incoherent areas away from the volcano, but reduces phase gradients or jumps on the rapidly deforming Mount Etna.

Unwrapping can be performed using the branch-cut algorithm of ROI_PAC (Goldstein et al., 1988), with pre-defined cuts imposed along the creeping Pernicana fault (Palano et al., 2006) and along some other minor structures, adjusted to observed phase jumps across coherent interferograms. Bridges across disconnected coherent areas are constructed by visual inspection of all interferograms. Alternatively, for study areas with lower coherence where a weighted sliding average has been employed on wrapped interferograms, we can use another unwrapper. The unwrapper also takes into account the cuts defined by ROI_PAC, but starts unwrapping the areas with the highest coherence, the coherence being computed during the preceding averaging filter step. When all connected areas with the highest coherence are unwrapped, the coherence threshold decreases. Every few iterations, the threshold is increased again, in order to always unwrap first areas with the highest possible coherence. Iterations continue until the lowest defined coherence threshold is reached. User defined bridges take precedence over the above-defined unwrapping path. This unwrapping procedure was chosen by Grandin et al. (2011) in their InSAR study across the Himalayas.

After unwrapping, empirical corrections of stratified atmospheric delays and/or residual orbit error may be re-estimated. Both contributions can then be inverted to ensure consistency in the interferometric network, before the final correction of these terms.

The phase dispersion spectrum, $D_l(x)$, of each interferogram l between master i and slave j dates, can then be estimated away from deforming areas, as a function of
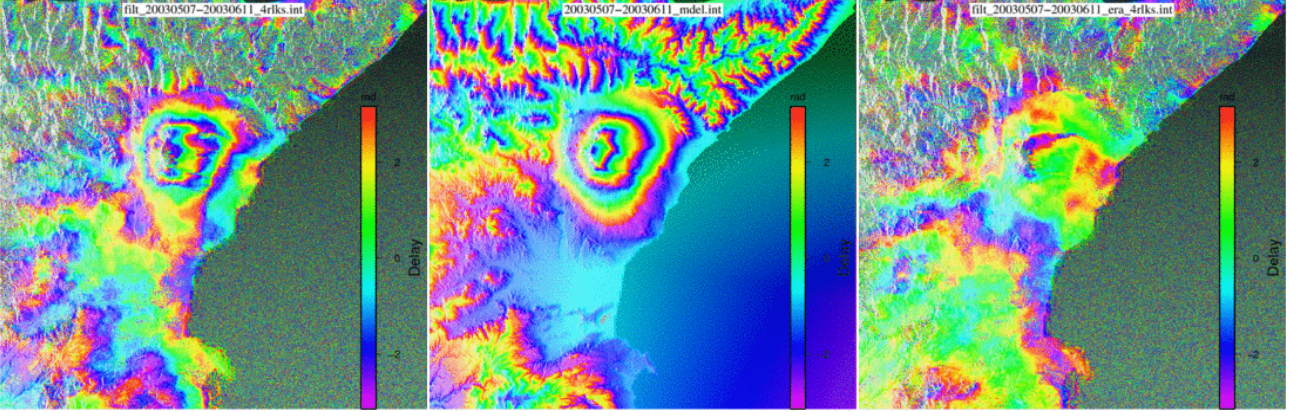
Figure 5. Example of an uncorrected interferogram (2003/05/07-2003/06/11), the stratified delay prediction based on ERAI (see ERAI points location on Fig. 2), and the corrected interferogram.

distance x (Cavalié et al., 2008):

$$D_l(x) = \frac{1}{n(x)} \sum_{|\vec{r_1}-\vec{r_2}|=x} |\Phi_l(\vec{r_1}) - \Phi_l(\vec{r_2})|$$

where $n(x)$ is the number of point pairs separated by a distance x, Φ_l is the interferometric phase, and $\vec{r_1}$ or $\vec{r_2}$ represent the points' positions. These values are inverted to quantify the amplitude of the phase dispersion (thus, the amplitude of the Atmospheric Phase Screen, APS), $D_k(x)$, of each image k as a function of distance x, using the approximate relation:

$$\forall l \in [1, M] \quad D_i(x) + D_j(x) = D_l(x) \qquad (1)$$

where M is the number of interferograms. This equation would be exact if D was refering to phase variance and if the covariance between two acquisitions' atmospheric phase screen was null. As turbulent APS patterns can be considered as random, their covariance must be small when the turbulent patterns spatial scale is small with respect to the study area. However, the chance of a non negligible covariance between turbulent APS patterns increases with the size of the APS patterns. Nevertheless, we verify that inversion of system (1) is stable when using for D phase dispersion, and for a redundant interferometric network. It yields quantitative information about the turbulent APS spectrum of each acquisition. Note that stratified APS and residual orbit must be removed before computing the interferogram phase dispersion, $D_l(x)$, as the amplitude of these terms does not obey equation (1) (their covariance is very large and cannot be neglected).

Finally, interferograms are referenced to a stable pixel or to stable areas.

4. TIME SERIES ANALYSIS AND TEMPORAL SMOOTHING

In the third step, the phase delays of unwrapped interferograms, Φ_l, are inverted pixel by pixel to solve for the total phase delay, φ_i, of each date relative to the first date,

whose delay, φ_1, is set to zero. The system is solved by least squares, regularization being provided by additional constraints (Lopez-Quiroz et al., 2009) instead of SVD inversion. The additional constraints are prescribed properties for the temporal evolution of the deformation, φ_k^s, (either smooth in time, or any parameterised function of time) plus a prescribed linear function of perpendicular baseline, $\Delta B_k^\perp$. The phase delay temporal evolution is obtained by solving the following equations for each pixel:

$$\forall l \in [1, M] \quad \varphi_j - \varphi_i = \Phi_l + \epsilon_l \qquad (2)$$

$$\varphi_1 = 0 \qquad (3)$$

$$\forall k \in [1, N] \quad \varphi_k - \varphi_k^s - \alpha \Delta B_k^\perp = E_k \qquad (4)$$

where N is the number of SAR images and α is the DEM correction term.

The error terms, ϵ_l and E_k, have a different meaning: they represent the interferometric network misclosure (i.e., mainly unwrapping errors), and unmodelled phase delay (i.e., mainly turbulent APS), respectively. Phase decorrelation noise, that does not "close" in the network (basically because of the effects of the adaptive range spectral filtering and of the spatial filter), also appears in ϵ_l as a secondary error source. The error E_k also includes phase decorrelation noise and deformation that does not follow the prescribed temporal evolution. Therefore, the APS amplitude, D_k, of each acquisition can be used to inversely weight the additional constraints (4). Similarly, lines (2) can be weighted by the average interferogram coherence, that can be expressed as a function of the interferogram temporal and spatial baseline. Furthermore, as unwrapping errors are expected to be independent between interferograms, one should set the data covariance between interferograms in (2) to zero, even if they have one common image. Similarly, as turbulent APS patterns are independent from one acquisition to the other, the data covariance between acquisitions in (4) is zero. We also make sure that the total weight on the set of equations (4) is set low enough relative to the total weight on set of equations (2), in order for lines (4) to only impact
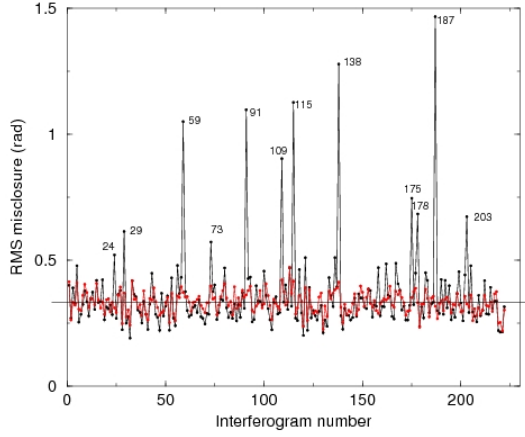
Figure 8. RMS misclosure for each interferogram (black without unwrapping error correction, red after automatic correction) to allow identification of unwrapping errors.

the relative phase delay between separated image subsets (Lopez-Quiroz et al., 2009).

When the prescribed properties for the temporal evolution of the deformation are given in the form of a parameterised function of time, the corresponding parameters are included and directly inverted in equation (4). Alternatively, when we only prescribe the deformation to be smooth in time, the smoothing can be obtained either by setting a temporal covariance on modelled φ_k^s (Jolivet et al., 2011c) or by adding lines minimizing the Laplacian of φ_k^s (Cavalié et al., 2007, as done here).
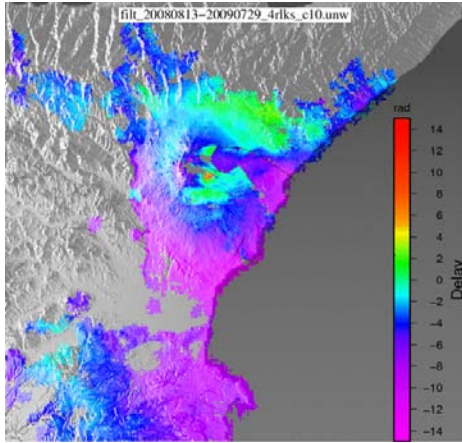

Figure 9. Unwrapped interferogram 187, presenting the highest residual (see Fig. 8).

A first run with a few iterations (weighted by the residue $|\epsilon_l|$) is performed to map inconsistencies in the interferometric network, thus detecting unwrapping errors (Fig. 8, 9, 10). A second run automatically corrects these unwrapping errors depending on the network redundancy. One example is provided here with an unwrapping error on interferogram 187 (Fig. 9), which peaks when one plots the global RMS misclosure of all interferograms

(Fig. 8). The misclosure map ϵ_l after a few iterations (Fig. 10) outlines the contour of the unwrapping error, bordered to the North by the Pernicana fault. The area with RMS close to 2π rad is then corrected, and the new misclosure map presents no notable discontinuities (Fig. 10).
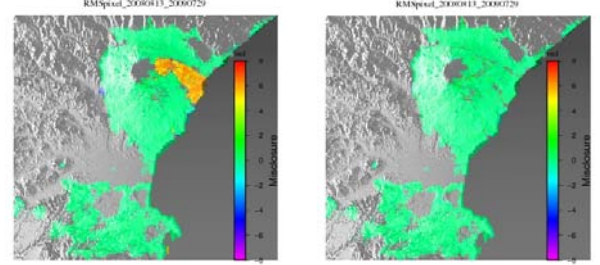

Figure 10. Interferometric misclosure maps for interferogram 187 before (left) and after (right) unwrapping error correction.

5. RESULTS OF THE ETNA VOLCANO STUDY

The output of the time series analysis consists of time series of total and smoothed phase delay (equations 2 and 4) for each pixel that is coherent for at least half the interferograms (Fig. 11). An averaged velocity map for the observation period is also given, together with the maps of other parameters optionally introduced in equation 4.
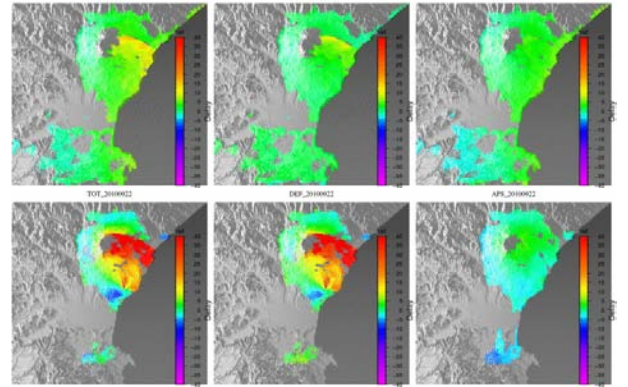

Figure 11. Snapshots for dates 20040107 (top) and 20100922 (bottom) showing the contribution to equation 4 of total phase φ_k, smoothed phase φ_s^k, and difference (APS).

The average velocity pattern presents strong similarities with that described by Bonforte et al. (2011) based on the ERS data set for the 1995-2000 period of time (Fig. 12) and is in agreement with their tectonic interpretation. The main feature is the motion away from the satellite of the east flank of Mount Etna, with relative velocity in the LOS of about 4 cm/yr. Non linear behavior of the deformation with time is also evident on the time series of a few points (Fig. 13). Relative displacements across the
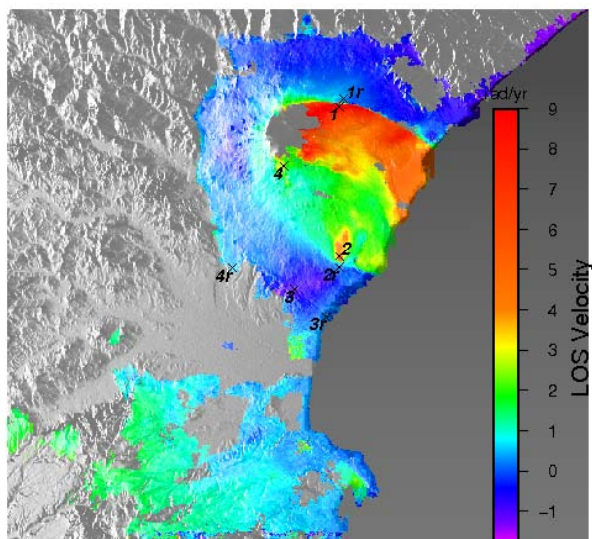
Figure 12. Map showing average velocity in rad/yr. X symbols and numbers indicate locations of pixels whose displacement evolutions are shown in Fig. 13.

Pernicana fault (point 1) show a progressive rate decay from about 15 cm/yr in early 2003 to a steady state velocity of ∼3 cm/yr in 2005-2009. A few events (in 2008 and 2010) are clearly visible in the raw time series. The displacement of point 2 away from satellite (probably subsidence) appears relatively steady state with a slowdown around 2007. A deformation pattern of lower amplitude, towards the satellite (possibly uplift), east of Catania is also clear (point 3) and corresponds to a mapped anticline, the Misterbianco ridge. Finally, we show the motion of a pixel (point 4) located on top of the volcano, on its southern part, with respect to a pixel South of the volcano, at low elevation. The pixel displays a progressive but irregular LOS delay increase (thus possible subsidence). The effect of the stratified atmospheric correction, using the ERAI atmospheric reanalysis, is also shown : The dispersion is clearly larger before ERAI correction.

6. CONCLUSION

In this paper, we present the main characteristics of the NSBAS chain, based on ROI_PAC (Rosen et al., 2004, http://www.openchannelsoftware.com/projects/ROI_PAC), that will be made available on http://www.efidir.fr in the coming months. Its development is based on a collaborative group of people and should continue over the coming years.

7. BIBLIOGRAPHY

Beauducel F., P. Briole, J.-L. Froger (2000). Volcano wide fringes in ERS SAR interferograms of Etna:
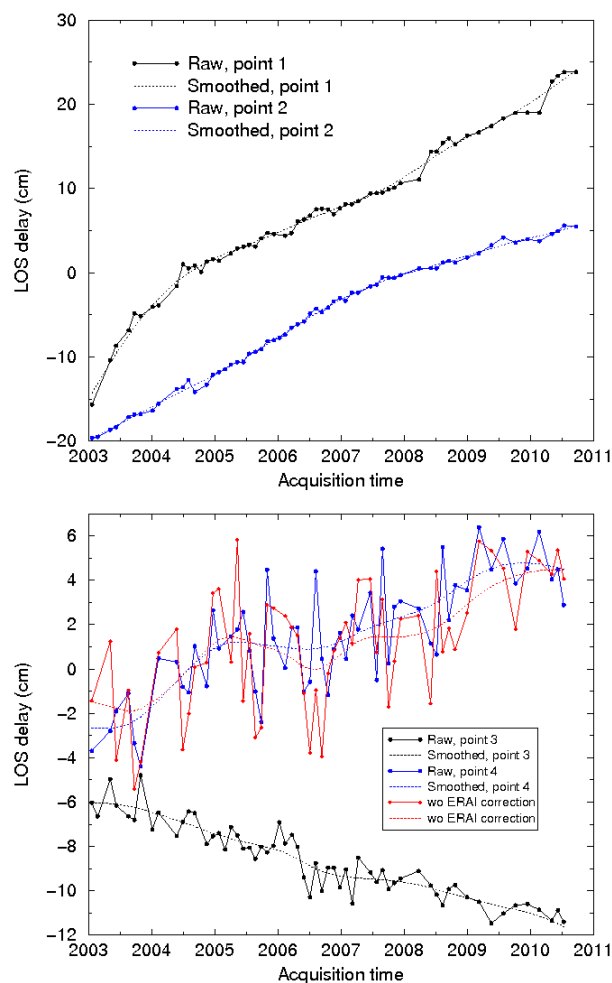
Figure 13. Displacement history of four pixels marked x on velocity map in Fig 12 relative to neighbouring pixels labeled with r. For pixel 4 the LOS delay evolution is shown with and without stratified atmospheric correction using ERAI model.

Deformation or tropospheric effect?. *J. of Geophys. Res.*, 105, 16391-16402, doi:10.1029/2000JB900095.

Berardino, P., G. Fornaro, R. Lanari, and E. Sansosti (2002). A new Algorithm for Surface Deformation Monitoring based on Small Baseline Differential SAR Interferograms. *IEEE Trans.Geosci. Remote Sens.* **40** (11), 2375-2383.

Bonforte A., F. Guglielmino, M. Coltelli, A. Ferretti, G. Puglisi (2011). Structural assessment of Mount Etna volcano from Permanent Scatterers analysis. *Geochem. Geophys. Geosyst.* 12, Q02002, doi:10.1029/2010GC003213.

Cavalié O., M.-P. Doin, C. Lasserre, P. Briole (2007), Ground motion measurement in the Lake Mead area, Nevada, by differential synthetic aperture radar interferometry time series analysis: Probing the lithosphere rheological structure, *J. Geophys. Res.*, 112, B03403, doi:10.1029/2006JB004344.

Cavalié O., C. Lasserre, M.-P. Doin, G. Peltzer, J. Sun, X. Xu and Z.-K. Shen (2008), Measurement of

interseismic strain across the Haiyuan fault (Gansu, China), by InSAR, *Earth and Planetary Science Letters*, 275, p 246-257, doi:10.1016/j.epsl.2008.07.057.

Doin M.-P., C. Lasserre, G. Peltzer, 0. Cavalié, C. Doubre (2009). Corrections of stratified tropospheric delays in SAR interferometry: validation with global atmospheric models, *J. of Applied Geophysics*, 69 (1), Sp. Iss. SI, 35-50, doi:10.1016/j.jappgeo.2009.03.010.

Ducret G., M. P. Doin, R. Grandin , C. Lasserre and S. Guillaso (2011). DEM corrections before unwrapping in a small baseline strategy for InSAR time series analysis. *Proc. Igarss.i, IEEE*, p 1353-1356

Goldstein R. M. and C. L. Werner (1998). Radar interferogram filtering for geophysical applications. *Geophys. Res. Lett.* **25** (21), 4035–4038.

Goldstein R. M. and H. A. Zebker and C. L. Werner (1988). Satellite radar interferometry : Two-dimensional phase unwrapping, *Radio Science*, 23, 713-720, doi: 10.1029/RS023i004p00713.

Grandin R., M-P Doin, L. Bollinger, B. Pnel-Puyssegur, G. Ducret, C. Lasserre (2011). Interseismic strain accumulation across an active thrust system: an InSAR case study in the Himalayas, Fringe, Frascati.

Guillaso S., C. Lasserre, M-P. Doin, O. Cavalié, J. Sun, G. Pelzer (2008). InSAR measurement of interseismic strain in areas of low coherence: example across the Haiyuan fault (Gansu, China) using a local InSAR adaptive range filter.*EGU,* **10**, A-09390.

Jolivet R., R. Grandin, C. Lasserre, M.-P. Doin, G. Peltzer (2011a). Systematic InSAR tropospheric phase delay corrections from global meteorological reanalysis data. *Geophys. Res. Lett.*, 38, pp.6.

Jolivet R., C. Lasserre , M-P Doin , S. Guillaso , G. Peltzer , R. Dailu , J. Sun , Z.-K. Shen , X. Xu, (2011b). Shallow creep on the Haiyuan Fault (Gansu, China) revealed by SAR Interferometry, Submitted to JGR

Jolivet R., C. Lasserre, M-P Doin, G. Peltzer, J. Sun, R. Dailu, Z-K Shen, X. Xiwei (2011c). Shallow creep along the Haiyuan fault (Gansu, China) revealed by InSAR time series analysis, Fringe, Frascati.

Lopez-Quiroz P., M.-P. Doin, F. Tupin, P. Briole, J.-M. Nicolas, Time series analysis of Mexico city subsidence constrained by radar Interferometry, *J. of Applied Geophysics*, 69 (1), Sp. Iss. SI, 1-15, doi: 10.1016/j.jappgeo.2009.02.006.

Palano M., M. Aloisi, M. Amore, A. Bonforte, F. Calvagna, M. Cantarero, O. Consoli, S. Consoli, F. Guglielmino, M. Mattia, B. Puglisi and G. Puglisi (2006). Kinematics and strain analyses of the eastern segment of the Pernicana Fault (Mt. Etna, Italy) derived from geodetic techniques (1997-2005), *Annals of geophysics*, 49, 1105-1117.

Rosen, P. A., S. Henley, G. Peltzer, and M. Simons (2004). Updated Repeat Orbit Interferometry Package Released. *Eos Trans*. AGU **85**(5), 47.